Hindawi
Advances in Materials Science and Engineering
Volume 2017, Article ID 7802024, 18 pages
https://doi.org/10.1155/2017/7802024

Research Article

Effect of Freeze-Thaw Cycles on the Internal Structure and Performance of Semirigid Base Materials

Yiqi Wang,[1,2] Yiqiu Tan,[1] Meng Guo,[3] and Xinglong Wang[4]

[1]*School of Transportation Science and Engineering, Harbin Institute of Technology, Harbin 150090, China*
[2]*College of Civil and Architectural Engineering, Heilongjiang Institute of Technology, Harbin 150050, China*
[3]*National Center for Materials Service Safety, University of Science and Technology Beijing, Beijing 100083, China*
[4]*Heilongjiang Institute of Highways and Transport Research, Harbin 150080, China*

Correspondence should be addressed to Yiqiu Tan; tanyiqiu@hit.edu.cn

Received 19 April 2017; Accepted 15 June 2017; Published 19 July 2017

Academic Editor: Giorgio Pia

In this study, we investigate the spatial distributions of the internal structures in semirigid base materials (SRBMs) and explore their effect on the service performance of the SRBMs. X-ray computed tomography (X-ray CT) was used to conduct a spatial voids structure analysis. Three variates were selected to study the factors influencing the spatial distributions of the internal structures, including freeze-thaw cycles, curing time, and cement content. The results show that, with the increase in the number of freezing and thawing cycles, the average porosity, void area, and void number of the SRBM samples increased, and the average void diameters of all samples initially increased and then decreased. These trends led to an increase in the mass loss ratio and strength loss ratio. Increasing the cement content and extending the curing time decreased the average number of voids, average void area, and average void diameter and decreased the mass loss ratio and strength loss ratio of the SRBMs. The top and bottom of the SRBM samples were more porous than the middle of the samples, whereas the maximum value of the average void diameter was observed in the middle of the samples.

1. Introduction

Semirigid base materials (SRBMs) are the most commonly used base materials for pavement in China. They are cost-effective materials with high stiffness and good moisture stability [1, 2]. SRBMs are porous materials made from inorganic binder stabilized aggregates after compaction process. The internal porous structure of SRBMs makes it easier to absorb water and moisture then ordinary concrete-like materials. When being used in cold region with freeze-thaw cycles, SRBMs will suffer the cyclic action of frozen-heave stress from the phase change of water until the internal structure failure [3]. Evolution of internal pore structure of SRBMs under freeze-thaw can be used as assessment criteria of frost resistance. Pavements that undergo freezing and thawing occupy 57% of the area in China. The frost resistance of the pavement base material is the most important property for pavement in China. The service life of the pavement is closely related to the freeze-thaw resistance of the SRBMs.

There are different methods for characterizing the internal structure of concrete. Łaźniewska-Piekarczyk studied the influence of the admixture type on the porosity and pore size distribution of high-performance self-compacting concrete (HPSCC) for a constant water-cement ratio, type and volume of aggregate, and volume of cement paste. He found that HPSCC was frost resistant even though the values of the air-void parameters differed from the standard recommendations [4]. Zeng et al. used experimental measurements and poroelastic approaches to assess the freeze-thaw behavior of air-entrained cement pastes saturated with 10 wt.% NaCl solutions and found that air-void entrainment tended to decrease the thermal contraction but increase the hydraulic expansion, ice nucleation expansion, and residual expansion [5]. Hazaree et al. studied the effects of variations in the cement content and air entrainment on the basic physical and mechanical properties and freeze-thaw resistance of roller-compacted concrete (RCC) mixtures and found that the physical and mechanical properties exhibited significant

Table 1: Specifications of the ordinary Portland cement type P.O42.5.

Properties	Specifications	Standard threshold
Stability (boiling method)	Qualified	—
Initial time (min)	165	≥90
Final setting time (min)	203	≤600
3 d		
Compressive strength (MPa)	26.4	≥17.0
Flexural strength (MPa)	5.87	≥3.5
28 d		
Compressive strength (MPa)	49.6	≥42.5
Flexural strength (MPa)	8.07	≥6.5

deviations from the behavior shown by conventional concrete. Air entrainment was found to affect the strength and freeze-thaw durability of the mixes [6]. Wawrzeńczyk and Kozak proposed a new description for the air-void structures in air-entrained concrete using a protected-paste volume (PPV) parameter. They found that, unlike other indicators representing a statistical estimation of the average spacing of air bubbles, the PPV better reflects the spatial displacement of air pores in concrete and can thus be considered a more suitable factor for air-void spatial dispersions [7]. Jin et al. proposed a fractal model to characterize the air-void size distributions in concrete and validated the corresponding fractal dimensions obtained from the fractal model to evaluate its effectiveness for quantitatively describing the air-void size distributions. They found that the air-void size distributions exhibited a more significant influence than the air-void spacing on the freeze-thaw resistance of concrete [8].

There is a correlation between the number of freeze-thaw cycles and the service performance of materials. Yan et al. investigated the effects of freeze-thaw cycles on the characteristics of stone mastic asphalt (SMA) mixtures containing cement (30%) or lime (20%) under different numbers of freeze-thaw cycles. They found that the initial air-void ratio played an important role in the performance of SMA under freeze-thaw cycles; the freeze-thaw resistance of the SMA mixtures with lime was better than that of the SMA mixtures with cement [9]. Gong et al. used a bending beam rheometer to investigate the low-temperature properties of fine aggregate matrixes (FAMs) and explored the effects of freeze-thaw cycles. They found that more air voids in the FAMs resulted in increased moisture damage, and this trend became more significant as the bath temperature increased [10]. Yi et al. developed a simple viscoelastic-plastic damage model to evaluate the effects of freeze-thaw cycles on porous asphalt mixtures. They found that loss of cohesion was the main failure mechanism in the porous asphalt mixtures under freeze-thaw cycles. Freeze-thaw effects also changed the plastic potential surface and induced large volumetric strains under loading [11]. The freeze-thaw cycles also damaged the interfacial adhesion between different materials and reduced the durability of the bulk materials [12–15].

Different technologies can be used to capture the internal structure of SRBMs. Guo et al. used a nondestructive ultrasonic scattering technique to determine the air-void size distribution in hardened concrete samples. They determined the air-void size distribution using an inverse analysis to minimize the difference between the theoretical and experimental attenuation of concrete [16]. Promentilla and Sugiyama used X-ray microtomography to characterize the internal structure of mortars that were exposed to freezing-thaw cycles and found that the initial air voids followed a lognormal distribution, with the largest population of the modal size occurring at approximately 30–50 μm, regardless of the type of mortar [17]. Xu et al. used X-ray computed tomography technology to capture the internal structure of samples before and after freeze-thaw tests and used a set of image analysis procedures for extracting the internal structure properties to analyze the changes in the air-void distributions and evaluate the internal structure evolution under freeze-thaw cycles. They found that the internal structure properties for the three types of asphalt mixtures differed from each other and resulted in various forms of internal structure evolution and microcrack formation under freeze-thaw cycles [18].

X-ray CT offers a novel way to study the internal structure of SRBMs and there was not much research in this field yet. The objectives of this research were to (1) study the spatial distributions of the internal structures in SRBMs and the relationships between the internal structure and service performance and (2) explore the influence of freeze-thaw cycles on the different internal structures and performance indicators of SRBMs.

2. Materials and Methods

2.1. Raw Materials and Mix Gradation. Ordinary Portland cement of type P.O42.5 was chosen, and its properties are listed in Table 1. The technical specifications of the aggregates used in the semirigid base material are shown in Table 2, and the aggregate grading curve is shown in Figure 1.

Aggregates, cement and water were mixed to prepare the SRBM samples. Three cement contents were selected: 4.0%, 4.5%, and 5.0%. The corresponding mixing proportions of three groups are shown in Table 3.

2.2. Specimen Preparation and Test Procedure

2.2.1. Sample Molding and Curing. According to the Manual for Highway Engineering Inorganic Binder Stable Material

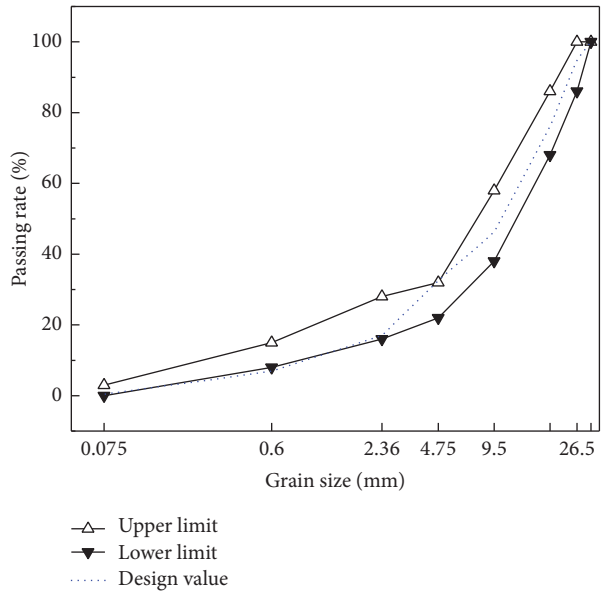

Figure 1: Grading curves of the cement stabilized macadam.

Table 2: Technical specifications of the aggregates.

Properties	Specifications	Standard threshold
Crushing value	13.73	<30%
Abrasion value	8.75	/
Liquid limit (%)	24	<28%
Plasticity index	8	6–9
Clay content (%)	1.76	/
Flat and elongated particles content (%)	5.85	<20%

Table 3: Mixing proportion of each group for per 100 kg aggregates.

Number	Aggregate (kg)				Cement (kg)	Water (kg)
	0~5 mm	5~10 mm	10~20 mm	20~30 mm		
1	27	13	30	30	4	5.24
2	27	13	30	30	4.5	6.26
3	27	13	30	30	5	5.49

Testing Procedures (JTG E51—2009) of China, the mixture ratio of the SRBM was determined based on the maximum dry density and optimum water content. Cylindrical specimens of Φ100 mm × 100 mm and Φ150 mm × 150 mm were fabricated using the static pressing method, while the former were prepared for X-ray CT tomography and the latter were for mass and strength loss ratio test. Three cement contents (4.0%, 4.5%, and 5.0%), two curing times (28 d and 90 d), and two types of freezing and thawing conditions (freezing and thawing and no freezing and thawing) were selected for this research. Nine replicate samples were prepared for each condition. In total, 108 samples were prepared. The mold was removed after 1 d of curing, and the sample was placed in a plastic bag after measuring the height, diameter, and weight. In addition, it was then kept in a standard curing room (20±2°C and ≥95% RH) for 28 and 90 d prior to testing.

2.2.2. Freeze-Thaw Cycle Experimental Procedure. After 28 or 90 d of curing, the samples were soaked in water with a temperature of 20 ± 2°C for 24 h, with the water surface maintained at a distance of 20 mm above the specimens. After soaking was completed, the samples were taken out of the water, and then, the weight, height, and diameter were measured. The sample was then kept in a −18°C cryogenic box for 16 h, after which the sample was placed in 20°C water to thaw for 8 h. During this thawing process, the water was 20 mm higher than the surface of the samples. The freeze-thaw cycles for 90 d occurred 0, 5, 10, 15, and 20 times. The freeze-thaw cycles for 28 d occurred 0, 5, and 10 times.

2.2.3. X-Ray Computed Tomography. In this study, X-ray CT (GE Phoenix, Germany) was used to capture digital images of the internal structures of the SRBMs. The X-ray CT (Figure 2)

(a) (b)

Figure 2: X-ray CT. (a) Exterior; (b) interior.

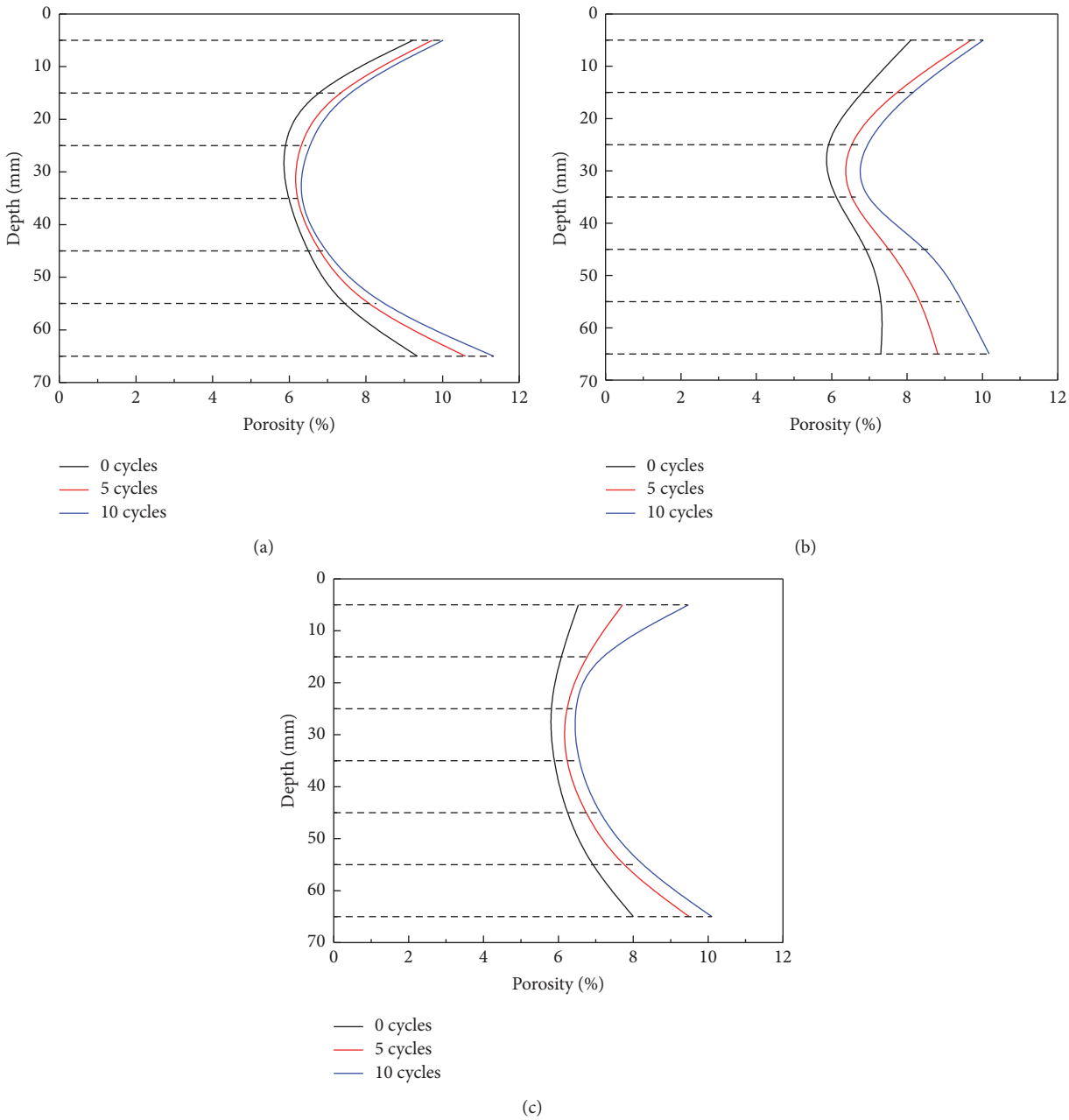

Figure 3: Porosity distributions of the different samples after 28 d of curing: (a) cement content = 4.0%; (b) cement content = 4.5%; (c) cement content = 5.0%.

Table 4: Specification parameters of the X-ray computed tomography.

Maximum voltage	240 kV
Maximum power	320 W
Detail resolution	1 μm
Minimum distance between the focal point and sample	4.5 mm
Maximum pixel resolution	<2 μm (3 d)
Geometrical magnification (2 d)	1.46~180 times
Geometrical magnification (3 d)	1.46~100 times
Maximum scan size (height × diameter)	420 mm × 135 mm
Maximum bearable weight	10 kg
Operation desk	Stable and flexible work station with 5 axles; high-precision turntable

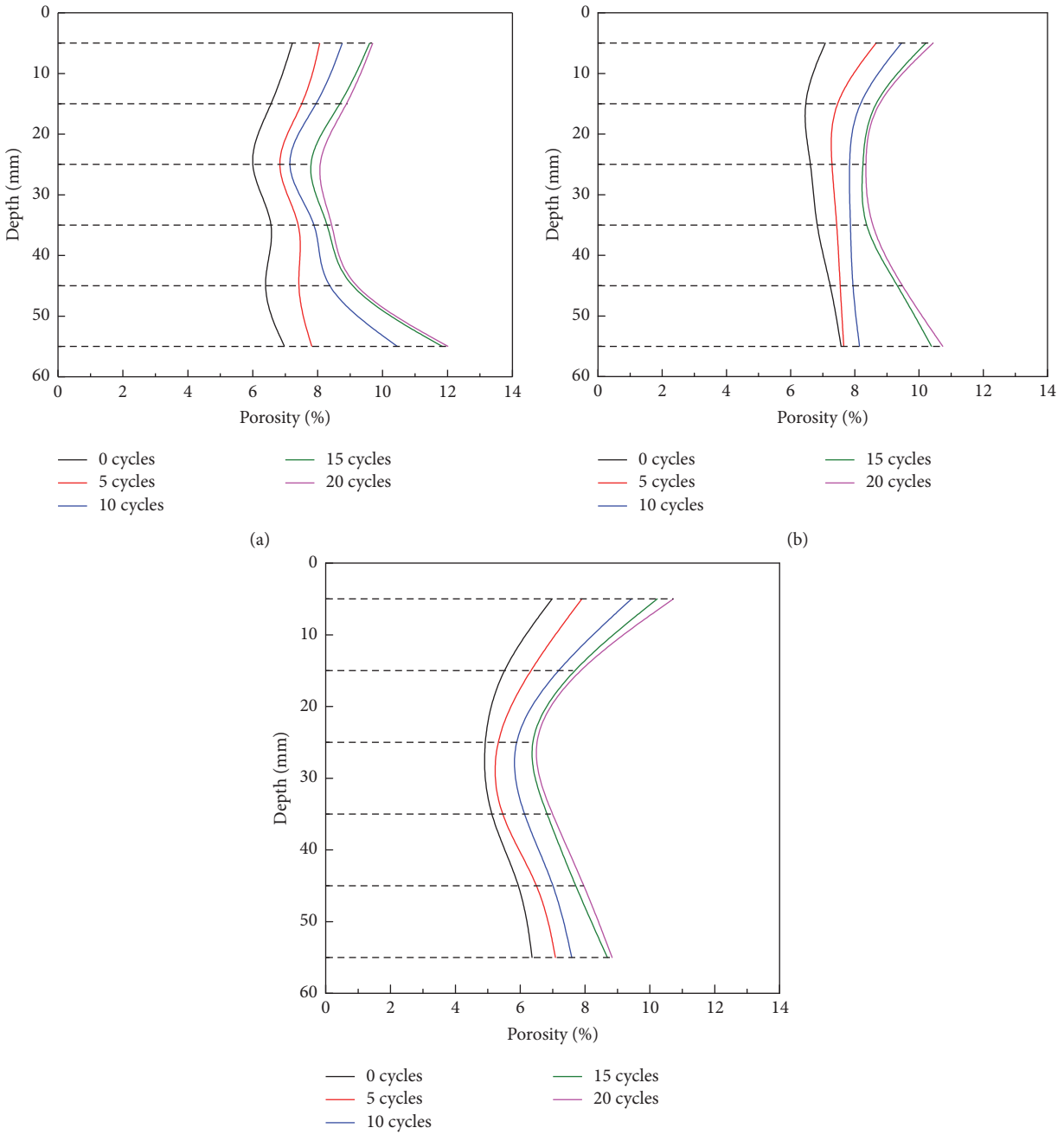

Figure 4: Porosity distributions of the different samples after 90 d of curing: (a) cement content = 4.0%; (b) cement content = 4.5%; (c) cement content = 5.0%.

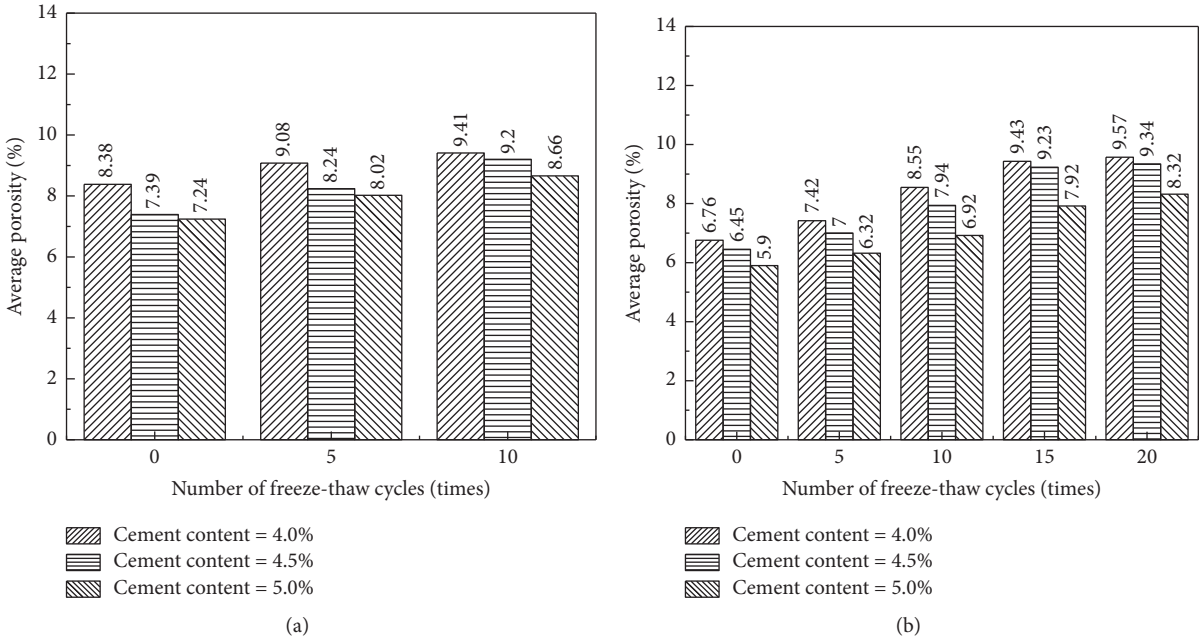

Figure 5: Effect of the freeze-thaw cycle number, cement content, and curing time on the average porosity: (a) curing time = 28 d; (b) curing time = 90 d.

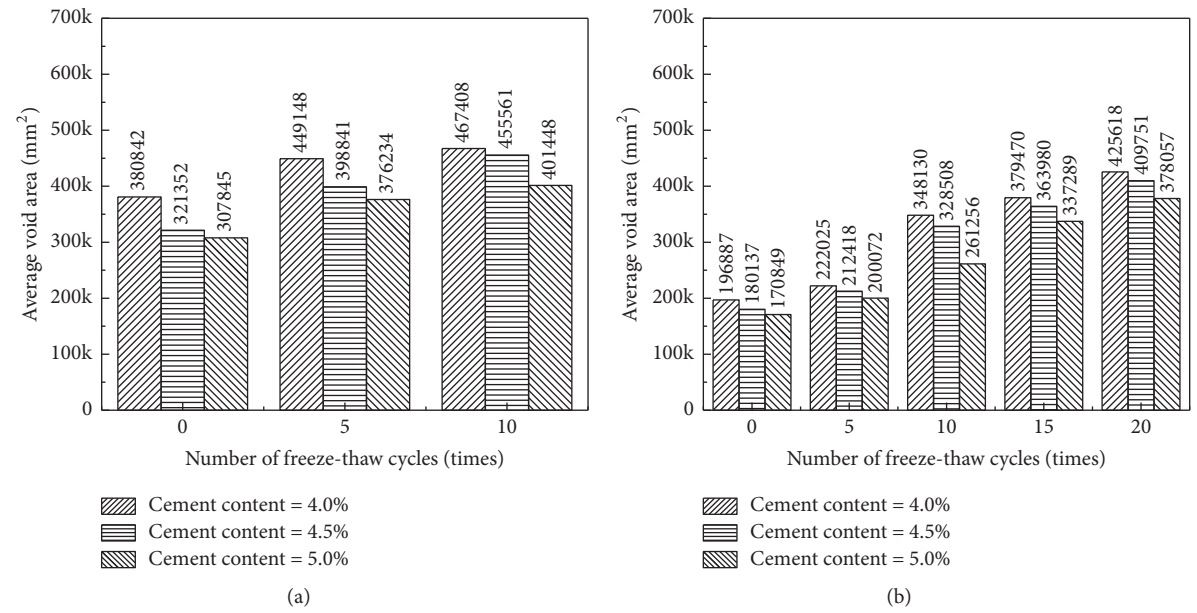

Figure 6: Effects of the number of freeze-thaw cycles, cement content, and curing time on the average void area: (a) curing time = 28 d; (b) curing time = 90 d.

machine has three main components, namely, the X-ray source, specimen position detectors, and X-ray intensity. The measured intensities are then converted to a map of the internal structure distribution in grayscale, which depends on the density and size of the object. Its specification parameters are provided in Table 4.

The specimens prepared for X-ray CT tomography should be pretreated before X-ray scanning. After the procedure of freeze-thaw cycles action, the feature of top and bottom of the specimens become rough, which has a strong impact on the verticality of specimen to the turntable of the instrument. In order to get the correct information of each scanning layer, a 10 ± 5 mm thick layer was sliced and removed from the top and bottom of the specimens, respectively. The height and volume of each specimen were measured and calculated accurately for pore parameters normalization processing.

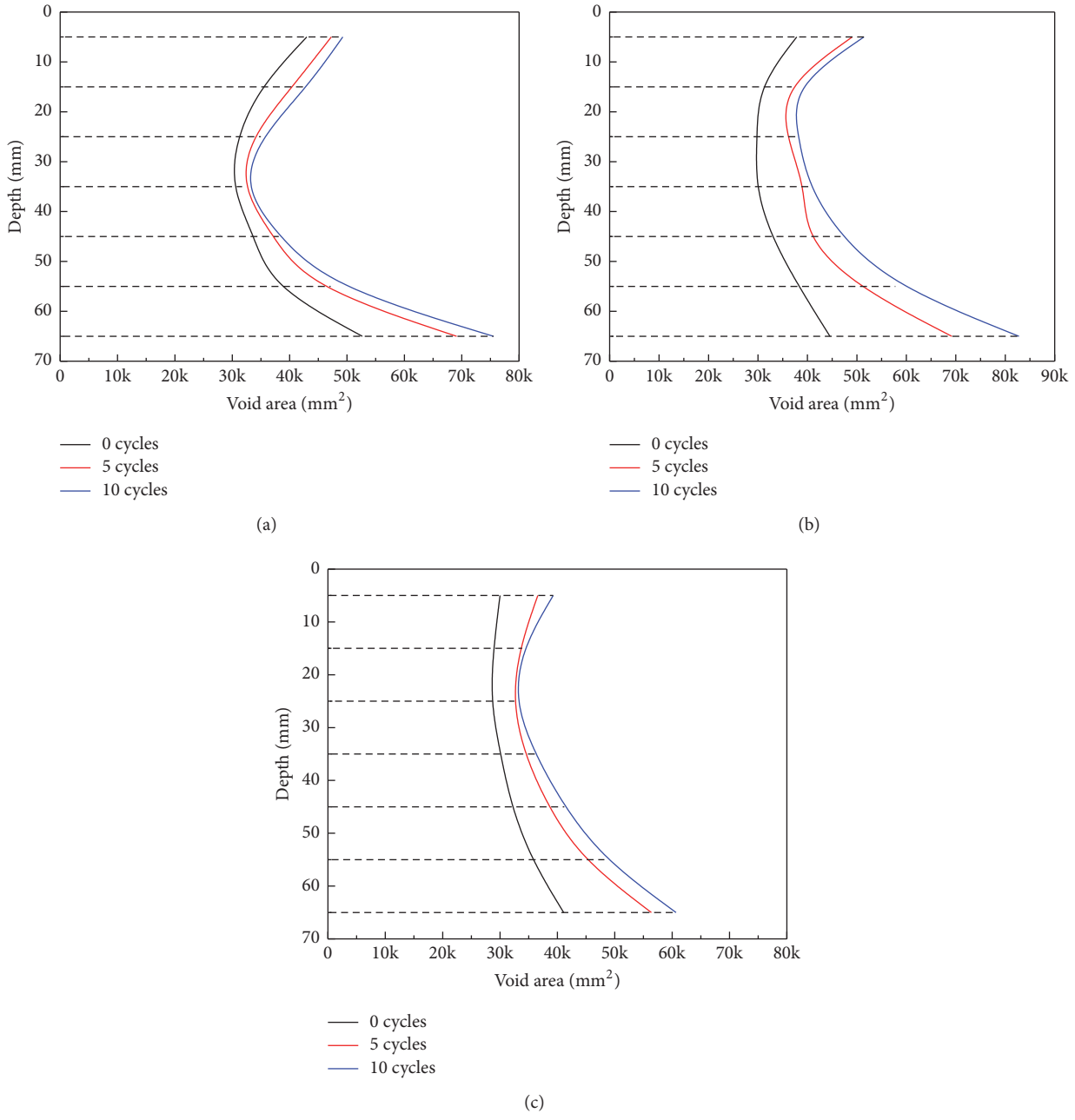

Figure 7: Distribution of the void areas of different samples after 28 d of curing: (a) cement content = 4.0%; (b) cement content = 4.5%; (c) cement content = 5.0%.

The operating process of the industrial CT was as follows:

(1) Start the X-ray generator, and select the preheat mode according to the breaking time.

(2) Start the computer, and operate the software. Use the Internet to build the connection.

(3) Put the pretreated sample on the turntable and immobilize it with matching kit.

(4) Select the scan parameters, and input the sample parameters into the system work station.

(5) Start the scan. A voltage of 200 kV and a current of 100 mA were selected to scan the SRBM.

(6) Adjust the integral time according to the sample size (1,000 ms).

(7) Select a proper number of projections. In this study, 1,000 layers of images were selected to reconstruct the sample.

The analysis software used was VGStudio MAX 3.0 (Volume Graphics). This software supports a variety of inputs

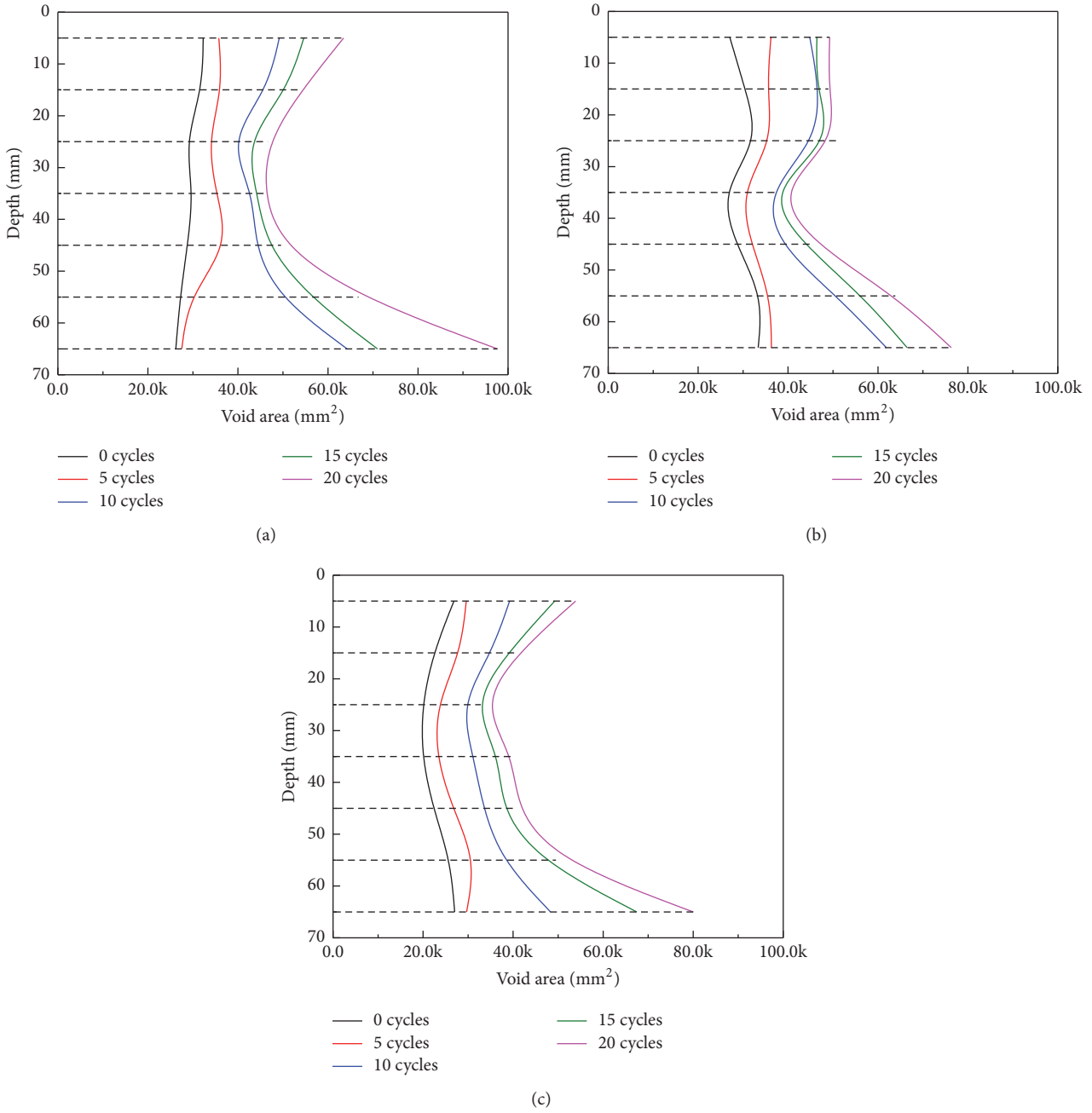

FIGURE 8: Distribution of the void areas of different samples after 90 d of curing: (a) cement content = 4.0%; (b) cement content = 4.5%; (c) cement content = 5.0%.

and outputs and can compound three-dimensional images. The average porosity and average pore diameter can be calculated according to the following equation:

$$\text{Average porosity} = \frac{\text{Air voids area}}{\text{Total image area}} \times 100$$
$$\text{Average pore diameter} = \sqrt{\frac{4 \times \text{Air pore area}}{\pi \times \text{Air pore number}}}. \quad (1)$$

2.2.4. Mass Loss Ratio. The mass loss is an important index of the damage level of SRBMs for evaluating the scaling phenomenon of a material suffering from freezing and thawing action and was calculated using the following equation:

$$W_n = \frac{m_0 - m_n}{m_0} \times 100, \quad (2)$$

where W_n is the mass loss ratio after n cycles (%), m_0 is the sample mass before the freezing and thawing cycles (g), and m_n is the sample mass after n freezing and thawing cycles (g).

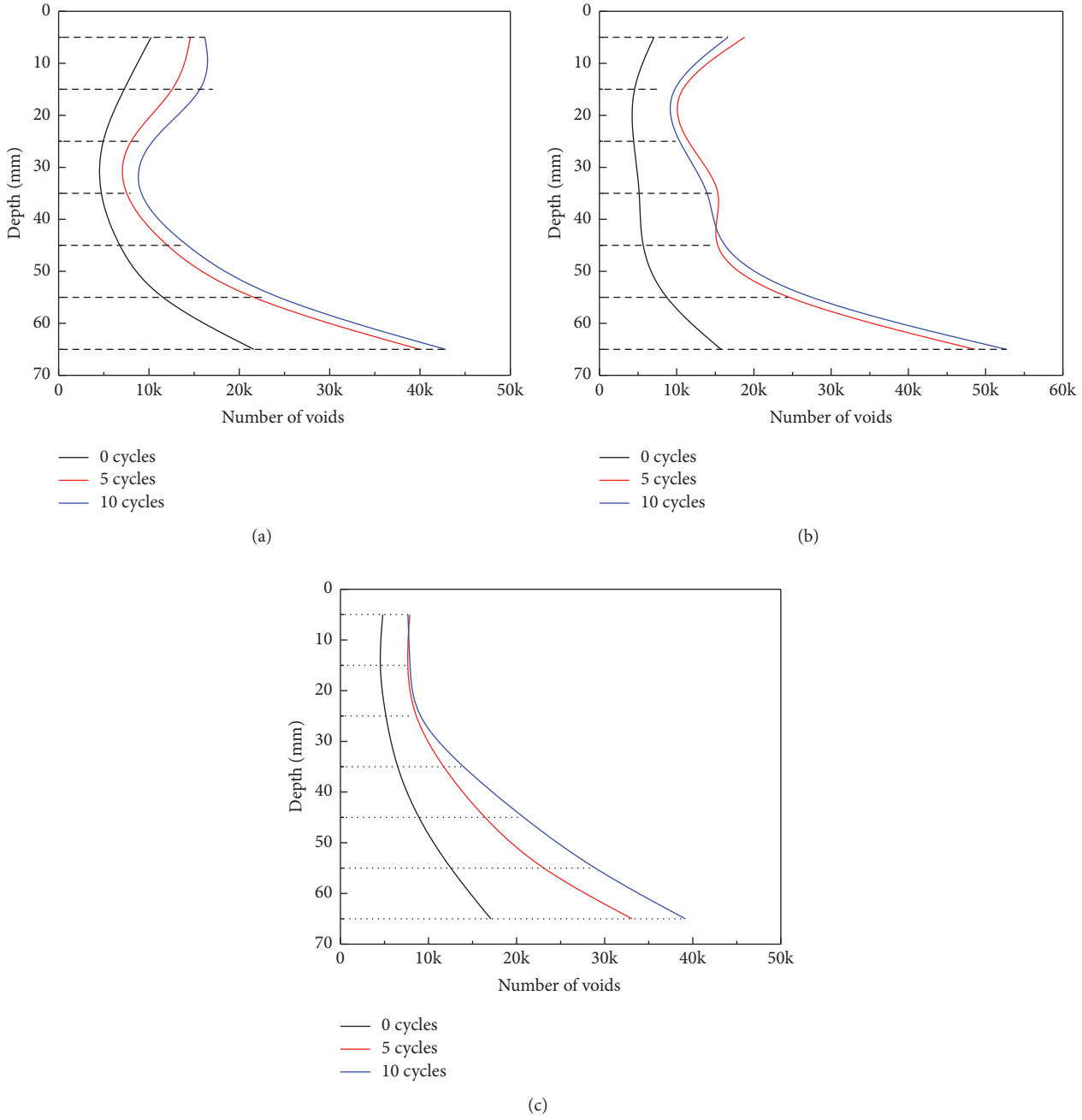

Figure 9: Void number distributions of different samples after 28 d of curing: (a) cement content = 4.0%; (b) cement content = 4.5%; (c) cement content = 5.0%.

2.2.5. Strength Loss Ratio. According to the Manual for Highway Engineering Inorganic Binder Stable Material Testing Procedures (JTG E51—2009) of China, UTM-250 (IPC Global, Australia) was adopted to test the compressive strength of the SRBM. The samples were placed on the vertical load center to avoid eccentric loading. A loading rate of 1 mm/min was applied on the samples, and the maximum damage pressure (P) was recorded. The unconfined compressive strength of the samples (R_c) was calculated using the following equation:

$$R_c = \frac{P}{A}, \tag{3}$$

where R_c is the unconfined compressive strength of the samples (MPa), P is the maximum damage pressure of the samples (N), A is the cross-sectional area of the samples (mm^2) ($A = \pi d^2/4$), and d is the diameter of the samples (mm).

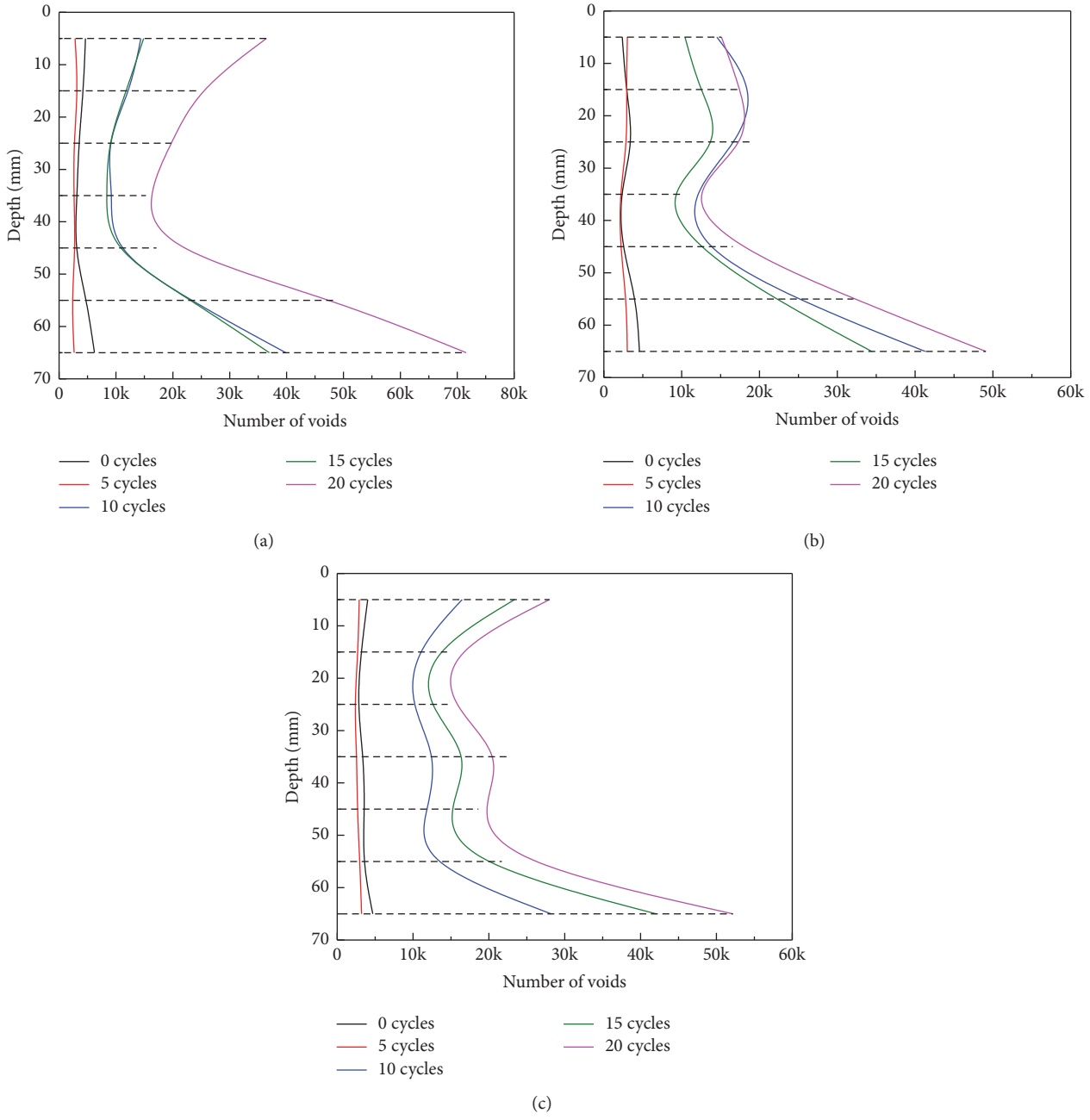

Figure 10: Void number distributions of different samples after 90 d of curing: (a) cement content = 4.0%; (b) cement content = 4.5%; (c) cement content = 5.0%.

3. Results and Discussion

3.1. Internal Structure

3.1.1. Porosity. X-ray computed tomography was used to capture the spatial information of the internal structures of the SRBMs, including the porosity, void area, and number of voids. The porosity distributions along the axial direction of the SRBM samples are shown in Figures 3 and 4.

Figures 3 and 4 illustrate that the porosities at the top and bottom of the SRBM samples were larger than that in the middle. The middle SRBM was more easily compacted, with a higher ratio mixture surrounding it. The difference in the porosity of the SRBM sample between different axial locations changed from 1% to 4%.

Figures 3 and 4 also show that the porosity of the SRBM sample increased with an increasing number of freeze-thaw cycles. However, the growth rate decreased with an increasing number of freeze-thaw cycles. The increment in the porosity was extremely small when the number of freeze-thaw cycles increased from 15 to 20 times. This result indicates that the degree of damage from the freeze-thaw cycles on the

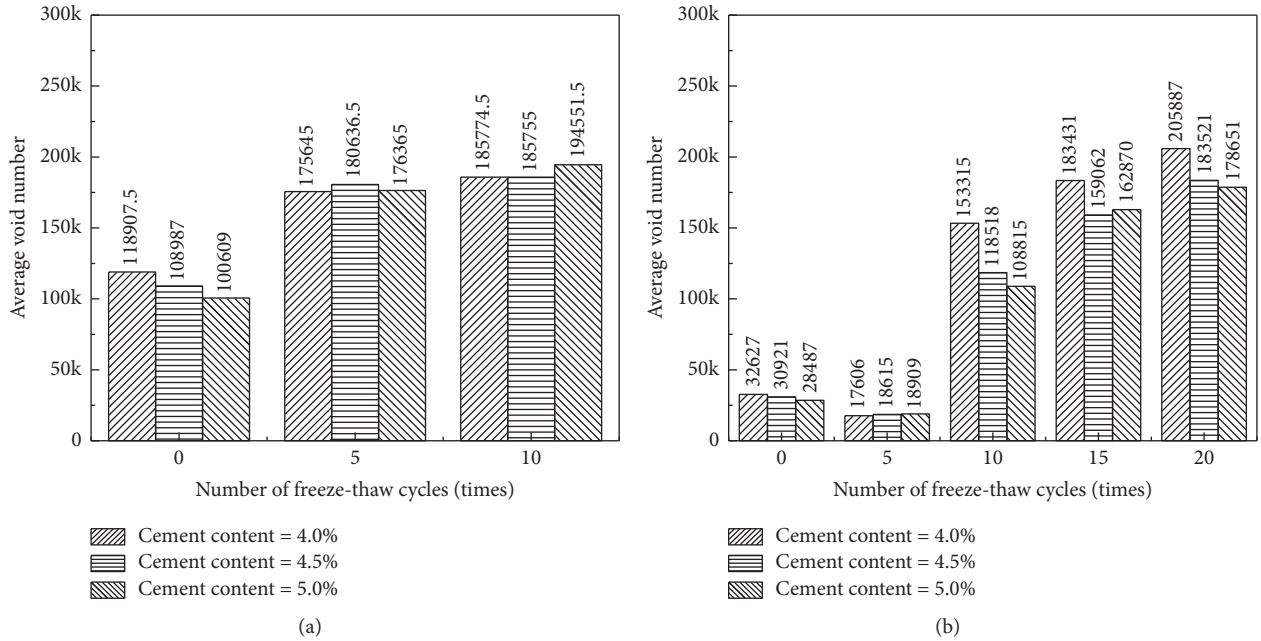

Figure 11: Effect of the number of freeze-thaw cycles, cement content, and curing time on the number of voids: (a) curing time = 28 d; (b) curing time = 90 d.

SRBM reached the maximum when the number of freeze-thaw cycles exceeded 15. After 15 cycles, additional freeze-thaw cycles only slightly damaged the internal structure of the SRBMs. The curing time had only a slight influence on the porosity distribution of the SRBMs. The performance of the SRBMs may have been improved by changing the microstructure or chemical composition. The average porosity of each sample is shown in Figure 5.

Figure 5 illustrates that the average porosity of the SRBM samples increased with an increasing number of freeze-thaw cycles. This trend was independent of the curing time. Figure 5 also shows that the samples with higher cement content had lower porosity. This indicates that increasing the cement content can help increase the compactness of SRBMs.

3.1.2. Void Area. The average void areas of each sample are shown in Figure 6. Figure 6 illustrates that the average void area increased with an increasing number of freeze-thaw cycles. The increase in the cement content led to a decrease in the average void area. A longer curing time led to a lower average void area of the sample.

The void area distributions along the axial direction of the SRBM samples are shown in Figures 7 and 8. Figures 7 and 8 illustrate that the void areas had similar trends to the porosity. The void areas and voids diameters may have determined the porosity. However, the accurate arithmetic of this relation requires further investigation.

3.1.3. Number of Voids. The void number distributions along the axial direction of the SRBM samples are shown in Figures 9 and 10.

Figures 9 and 10 illustrate that the number of voids initially decreased and then increased with increasing scan depth. The number of voids was minimal when the scan depth was approximately 20–30 mm. With an increase in the number of freeze-thaw cycles, the number of voids increased but the increasing rate decreased. For the sample with a cement content of 4.5%, the number of voids did not change significantly when the number of freeze-thaw cycles increased from 5 to 10 times. Compared to the samples with 28 d of curing, the changes in the number of voids for the samples with 90 d of curing were more interesting. For the samples with 90 d of curing, the number of voids was nearly the same along the axial direction when the number of freeze-thaw cycles was less than 5. However, when the number of freeze-thaw cycles was more than 10, the number of voids started to increase significantly, particularly for the top and bottom parts of the SRBM samples. The void number distributions along the axial direction were nearly the same as those of the porosity when the number of freeze-thaw cycles was more than 10. The number of voids also increased with an increase in the number of freeze-thaw cycles. The average number of voids of each sample is shown in Figure 11.

As shown in Figure 11, the average number of voids in the samples increased with an increase in the number freeze-thaw cycles. The rate of increase reached the maximum when the freeze-thaw cycle number was 5 (28 d of curing) and 10 (90 d of curing). The rate of increase in the average number of voids became slower when the freeze-thaw cycle number increased further. Figure 11 illustrates that higher cement content helped to reduce the average number of voids in the bulk samples, except for certain cases, such as the samples

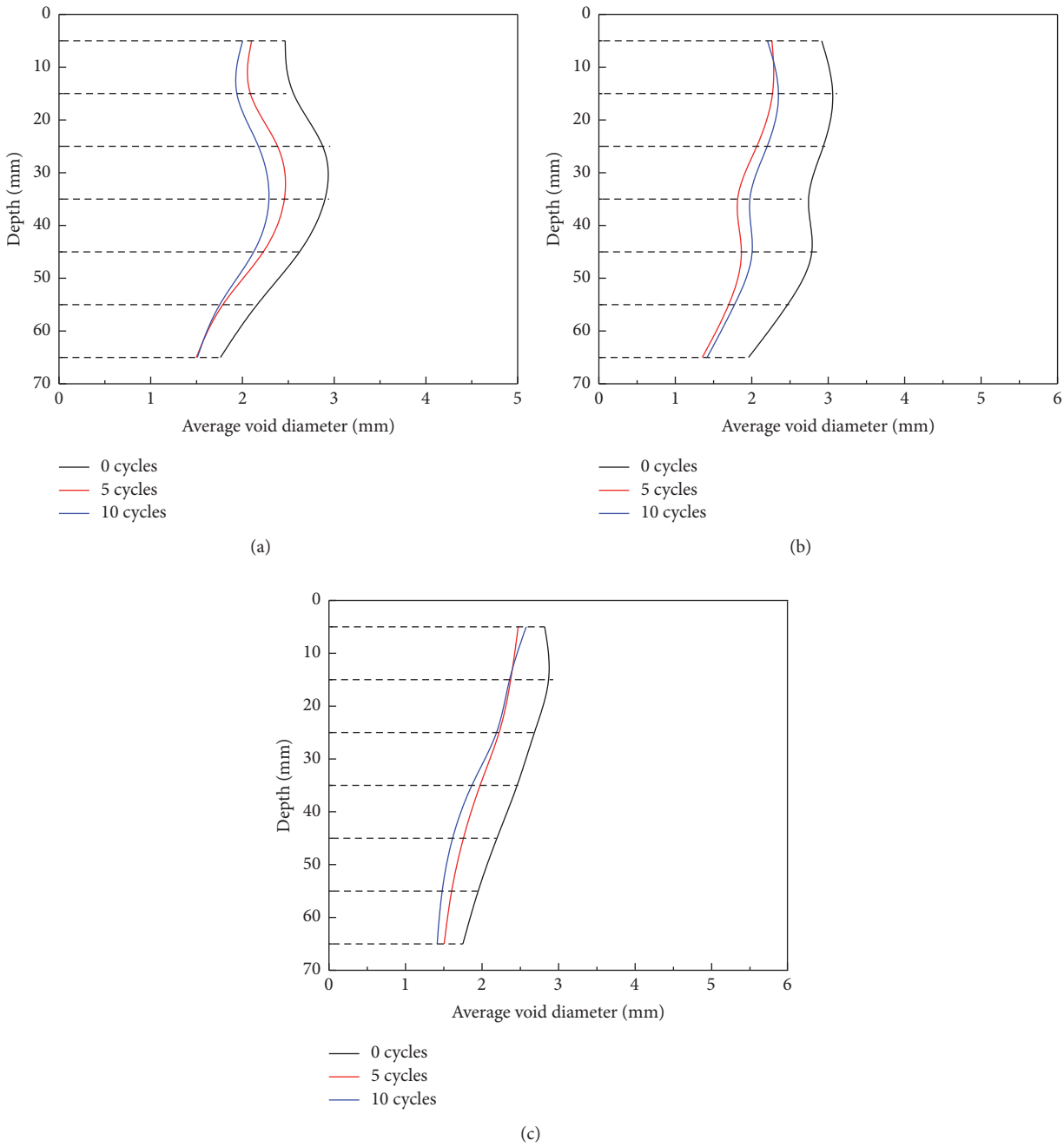

Figure 12: Average void diameter distributions of the different samples after 28 d of curing: (a) cement content = 4.0%; (b) cement content = 4.5%; (c) cement content = 5.0%.

subjected to 5 freeze-thaw cycles and 28 d of curing. This small variation may have been due to experimental error. A comparison of the results between 28 d and 90 d of curing illustrates that a longer curing time led to a higher average number of voids in the bulk samples. This indicates that extending the curing time can enhance the adhesion strength and cohesion strength of SRBMs, resulting in an increase in the freeze-thaw cycle resistance ability.

3.1.4. Average Void Diameter. The void number distributions along the axial direction of the SRBM samples are shown in Figures 12 and 13.

Figures 12 and 13 illustrate that the average void diameter of the SRBM samples had a different trend than the porosity and number of voids. For the samples with a cement content of 4.0%, the maximum value of the average void diameter was located in the middle of the sample. For the other samples,

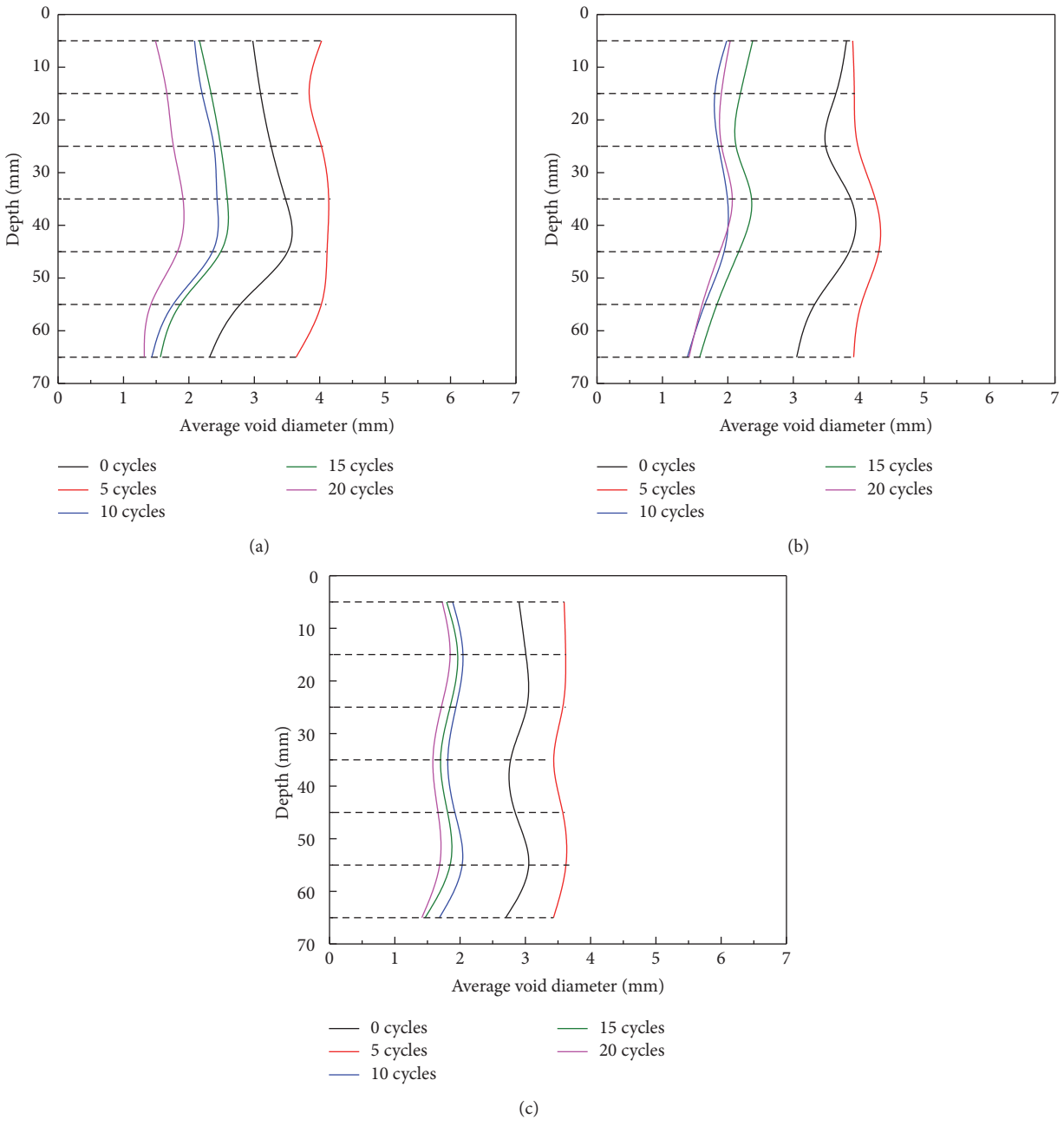

Figure 13: Average void diameter distributions of the different samples after 90 d of curing: (a) cement content = 4.0%; (b) cement content = 4.5%; (c) cement content = 5.0%.

the maximal average void diameter was also located near the middle of the sample. The middle part of the samples was more protected by the surrounding aggregates. However, the top and bottom of the samples suffered more direct compaction pressures from the metal mold when the sample was compacted.

Figures 12 and 13 also illustrate that the average void diameters became considerably smaller when the number of freeze-thaw cycles increased to more than 10. When the curing time was 28 d, the second set of five freeze-thaw cycles had a lesser influence than the first set. When the curing time was 90 d, the first set of five freeze-thaw cycles had an opposite influence, and the average void diameter decreased rapidly. This behavior occurs because the first set of five freeze-thaw cycles increased the void diameter by the frost heave action of the ice, and the following freeze-thaw cycles damaged the unstable large voids, creating smaller voids. The average void diameter of each sample is shown in Figure 14.

In Figure 14, the average void diameter of each sample decreased with increases in the cement content. An increase

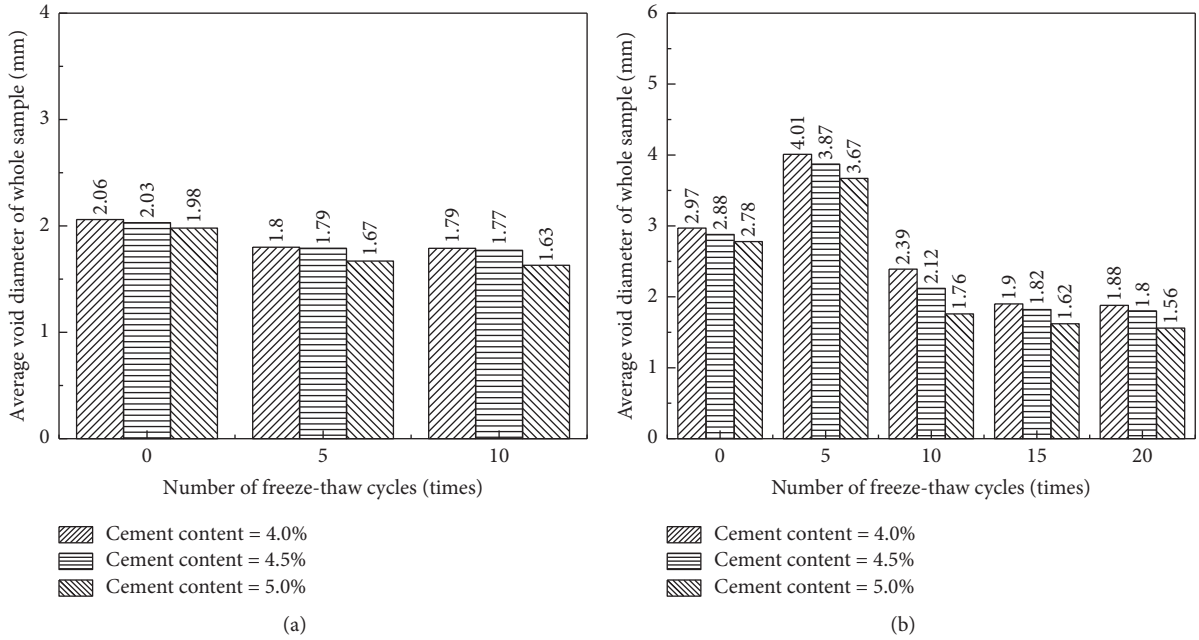

Figure 14: Effect of the number of freeze-thaw cycles, cement content, and curing time on the average void diameter of the sample: (a) curing time = 28 d; (b) curing time = 90 d.

in the number of freeze-thaw cycles also led to the same trend, except for the case of 5 cycles and a curing time of 90 d.

3.1.5. Horizontal Observation of the Internal Structure Changes in the SRBMs. Based on the above quantitative analysis, the internal structure changes of the SRBM samples were clearly recognized along the longitudinal direction. However, the distribution of the internal structure along the horizontal direction required further characterization. This section describes the distributions of the internal structures at three locations. The change in the internal structures with an increasing number of freeze-thaw cycles was analyzed. The results are shown in Figures 15 and 16.

Different colors in these two figures represent the voids generated at different time. Blue represents the initial void distribution prior to the freeze-thaw cycles, red represents the increased voids after 5 freeze-thaw cycles, and black represents the increased voids from 5 to 10 freeze-thaw cycles.

There are three location marks in the figures. "Top" represents the layer within a 1 cm distance from the top surface of the sample, "bottom" represents the layer within a 1 cm distance from the bottom surface of the sample, and "middle" represents the middle layer of the sample.

Some conclusions from the above analysis can be demonstrated qualitatively from Figures 15 and 16. The top and bottom of the samples had smaller and more abundant voids. In addition, the rate of increase was considerably faster. Higher cement content led to a lower void area. Longer curing times also helped to decrease the void area.

3.2. Mass Loss Rate. The mass loss rates of the samples with different cement dosages and at different curing ages are shown in Figure 17.

Figure 17 shows that the mass loss ratios increased with an increasing number of freezing and thawing cycles. However, the increase rate decreased with an increasing number of freezing-thawing cycles. The increment from the 15th to 20th cycle was nearly half of that from the 5th to 10th cycle. This trend is due to water entering the voids of the samples and damaging the samples by glaciation. However, glaciation damage was limited. After the weak parts of the samples were damaged, it was difficult for void water glaciation to damage the other stronger parts. Therefore, the increment in the mass loss rate decreased with an increasing number of freeze-thaw cycles.

The mass loss ratios of samples cured for 90 d were less than those of the samples cured for 28 d, indicating that extending the curing time could improve the freeze-thaw resistance of SRBMs. The mass loss ratio also exhibited a decreasing trend with increases in the cement content, indicating that increasing the cement content can improve the freeze-thaw resistance of SRBMs.

3.3. Strength Loss Rate. The strength loss rates of samples with different cement dosages and different curing times are shown in Figure 18.

In Figure 18, the strength loss rates increased with an increasing number of freeze-thaw cycles but decreased with increasing curing time. The same trends occurred for the

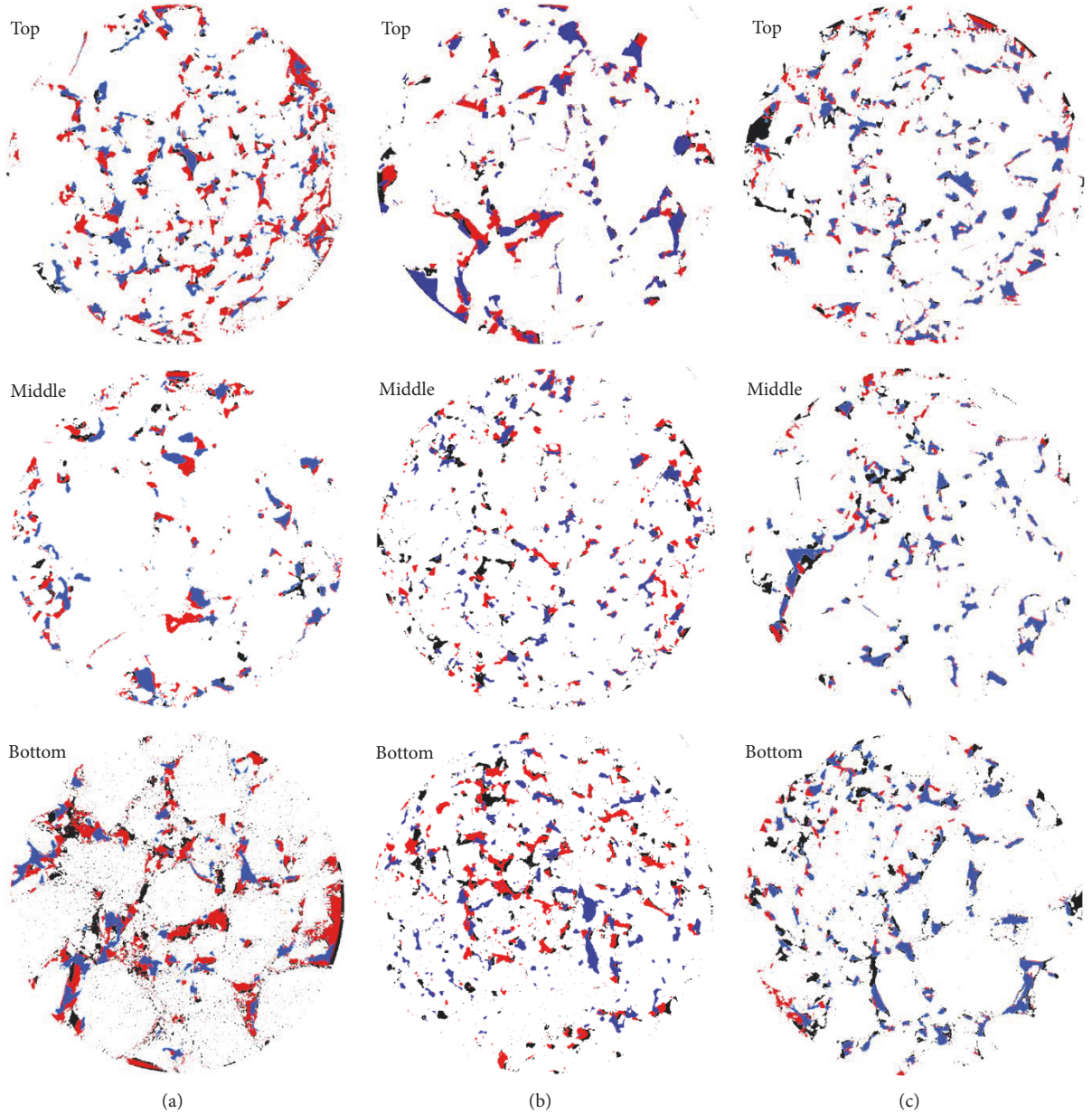

FIGURE 15: Change of the internal structures of the SRBM samples along the horizontal direction when the curing time was 28 d: (a) cement content = 4.0%; (b) cement content = 4.5%; (c) cement content = 5.0%.

mass loss rate, indicating that the freeze-thaw cycles could damage the SRBMs. The degree of damage was greatest during the first freeze-thaw cycle and decreased with an increasing number of freeze-thaw cycles.

Figure 18 illustrates that the strength loss rate of the SRBM samples decreased with increasing cement content. This result indicates that increasing the content of the cement can improve the performance of the SRBM samples. This may be attributed to the cement content decreasing the air voids of the SRBMs. The degree of damage from the freeze-thaw cycles decreased with a decreasing number of air voids.

4. Conclusions

The objective of this study was to investigate the spatial distributions of the internal structures of SRBMs and their effect on the service performance. X-ray computed tomography was used to analyze the effects of the number of freeze-thaw cycles, curing time, and cement content on the internal structures. The following conclusions can be drawn based on the aforementioned results and discussion:

(1) The mass loss ratio and strength loss ratio of the SRBM samples increased with an increase in the number of freezing and thawing cycles.

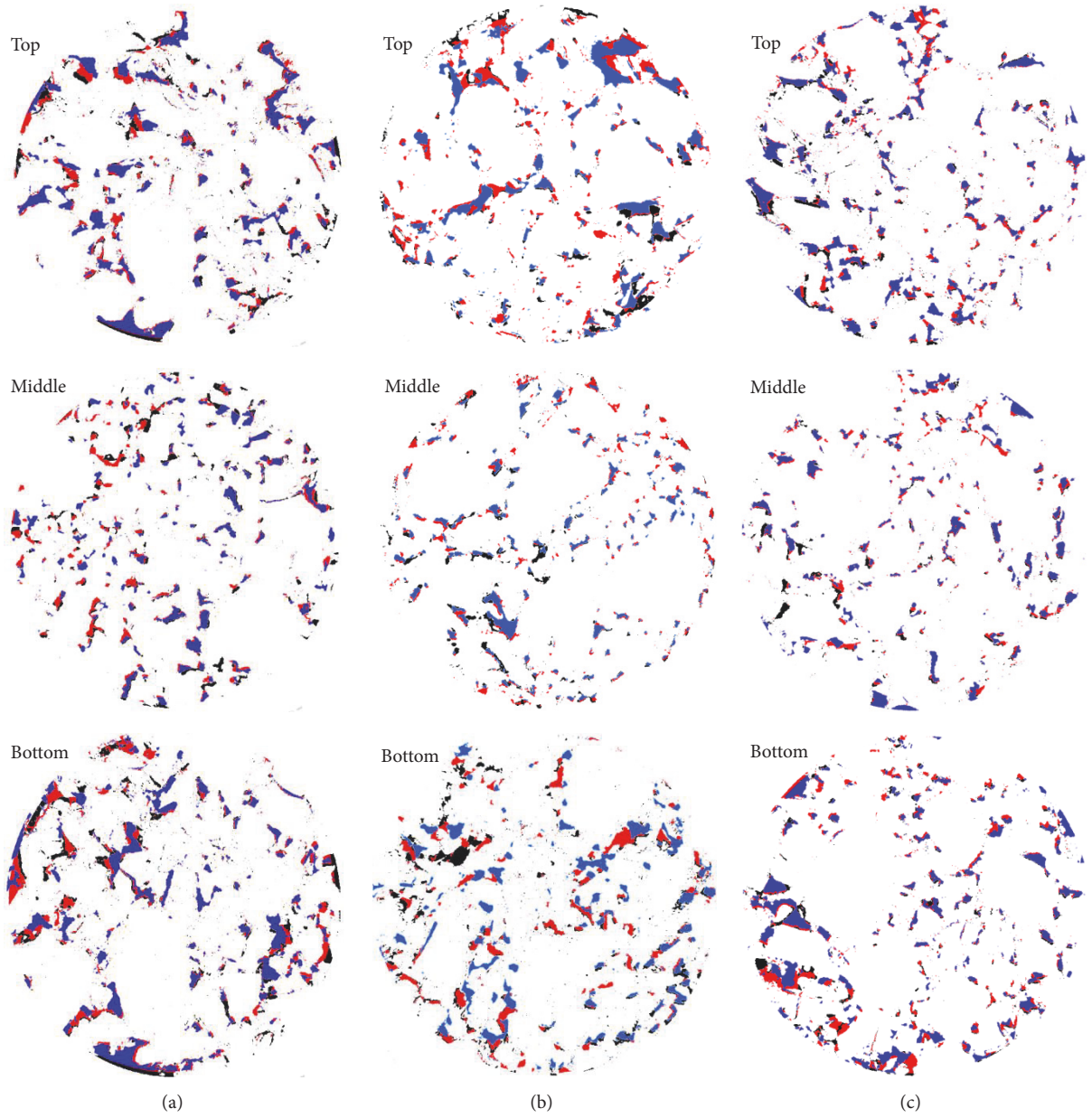

Figure 16: Change of the internal structures of the SRBM samples along the horizontal direction when the curing time was 90 d: (a) cement content = 4.0%; (b) cement content = 4.5%; (c) cement content = 5.0%.

(2) Increasing the cement content and the curing time reduced the mass loss ratio and strength loss ratio of the SRBMs.

(3) The porosity of the top and bottom of the SRBM samples was larger than that in the middle. The average porosity of the SRBM samples increased with an increase in the number of freeze-thaw cycles. The samples with a higher cement content were less porous.

(4) The number of voids and void areas increased with an increasing number of freeze-thaw cycles. Extending the curing time or increasing the cement content reduced the average number of voids and average void area of the samples.

(5) The maximum value of the average void diameter was located near the middle of the samples. The initial freeze-thaw cycles increased the average void diameters of the SRBM samples due to the effect of ice frost heaving. The average void diameter of the sample will decrease with an increasing number of freeze-thaw cycles because the large voids will become smaller voids. Extending the curing time decreased the average void diameter.

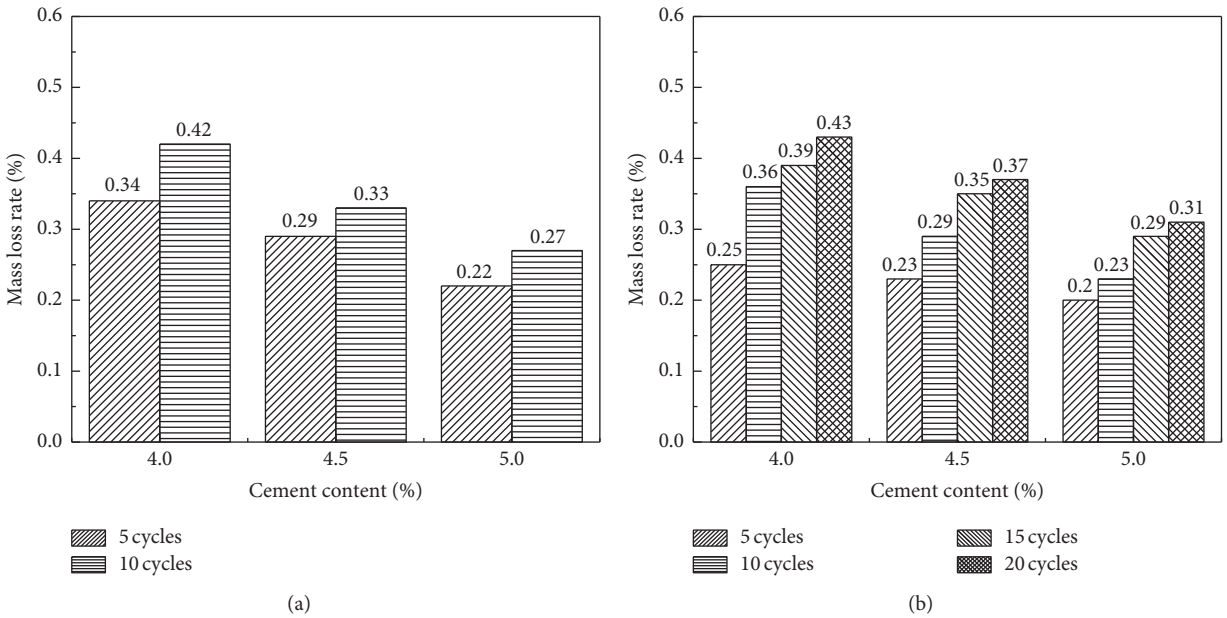

Figure 17: Mass loss rates of the SRBM after different numbers of freeze-thaw cycles: (a) curing time = 28 d; (b) curing time = 90 d.

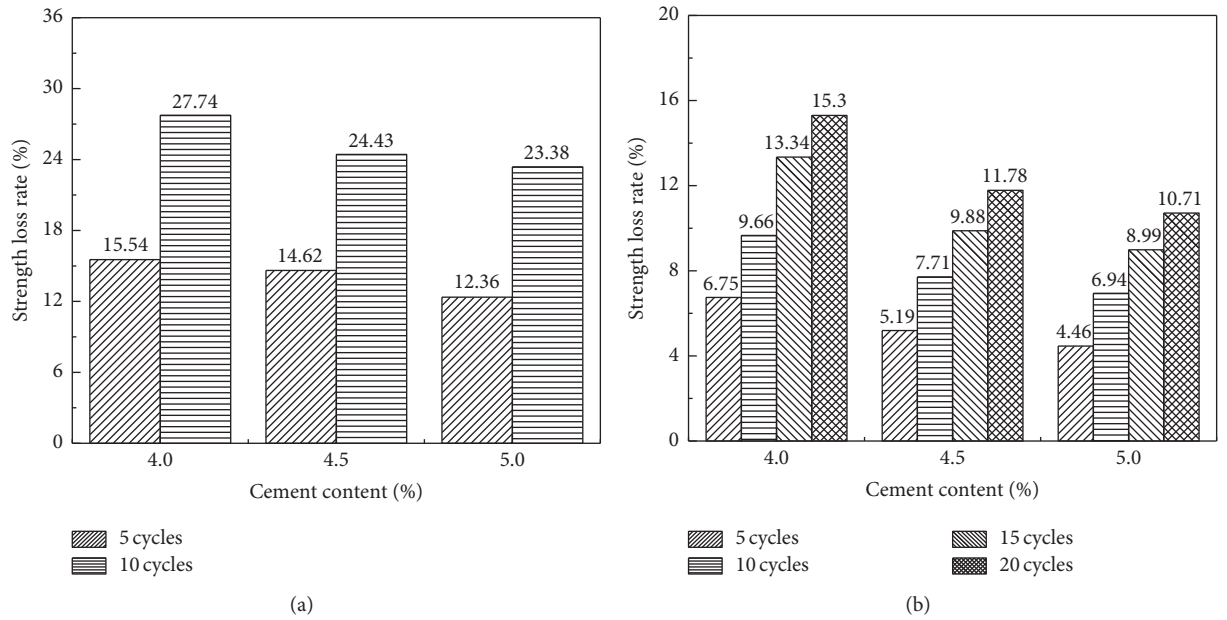

Figure 18: Strength loss rates of the SRBMs after different numbers of freeze-thaw cycles: (a) curing time = 28 d; (b) curing time = 90 d.

Conflicts of Interest

The authors declare no conflicts of interest.

Authors' Contributions

Yiqi Wang and Yiqiu Tan conceived and designed the experiments; Yiqi Wang performed the experiments; Yiqi Wang and Xinglong Wang analyzed the data; Yiqi Wang and Meng Guo wrote the paper.

Acknowledgments

This study was funded by the Natural Science Foundation of Beijing, China (Grant no. 8174071), and the China Postdoctoral Science Foundation (Grant no. 2016M600926). The

authors are also grateful to the Department of Transportation in Heilongjiang Province for their support of this work.

References

[1] J. Zheng, "Design guide for semirigid pavements in china based on critical state of asphalt mixture," *Journal of Materials in Civil Engineering*, vol. 25, no. 7, pp. 899–906, 2013.

[2] A. M. Sha, "Material characteristics of semi-rigid base," *China Journal of Highway and Transport*, vol. 21, pp. 1–5, 2008.

[3] T. C. Powers and R. A. Helmuth, "Theory of volume changes in hardened portland cement paste during freezing," *Highway Research Board Proceedings*, vol. 32, pp. 285–297, 1953.

[4] B. Łaźniewska-Piekarczyk, "The frost resistance versus air voids parameters of high performance self compacting concrete modified by non-air-entrained admixtures," *Construction and Building Materials*, vol. 48, pp. 1209–1220, 2013.

[5] Q. Zeng, L. Li, X. Pang, Q. Gui, and K. Li, "Freeze-thaw behavior of air entrained cement paste saturated with 10 wt.% NaCl solution," *Cold Regions Science and Technology*, vol. 102, pp. 21–31, 2014.

[6] C. Hazaree, H. Ceylan, and K. Wang, "Influences of mixture composition on properties and freeze-thaw resistance of RCC," *Construction and Building Materials*, vol. 25, no. 1, pp. 313–319, 2011.

[7] J. Wawrzeńczyk and W. Kozak, "Protected Paste Volume (PPV) as a parameter linking the air-pore structure in concrete with the frost resistance results," *Construction and Building Materials*, vol. 112, pp. 360–365, 2016.

[8] S. Jin, J. Zhang, and B. Huang, "Fractal analysis of effect of air void on freeze-thaw resistance of concrete," *Construction and Building Materials*, vol. 47, pp. 126–130, 2013.

[9] K. Yan, D. Ge, L. You, and X. Wang, "Laboratory investigation of the characteristics of SMA mixtures under freeze-thaw cycles," *Cold Regions Science and Technology*, vol. 119, pp. 68–74, 2015.

[10] X. Gong, P. Romero, Z. Dong, and D. S. Sudbury, "The effect of freeze-thaw cycle on the low-temperature properties of asphalt fine aggregate matrix utilizing bending beam rheometer," *Cold Regions Science and Technology*, vol. 125, pp. 101–107, 2016.

[11] J. Yi, S. Shen, B. Muhunthan, and D. Feng, "Viscoelastic-plastic damage model for porous asphalt mixtures: Application to uniaxial compression and freeze-thaw damage," *Mechanics of Materials*, vol. 70, pp. 67–75, 2014.

[12] M. Guo, A. Motamed, Y. Tan, and A. Bhasin, "Investigating the interaction between asphalt binder and fresh and simulated RAP aggregate," *Materials and Design*, vol. 105, pp. 25–33, 2016.

[13] S.-H. Lee, K.-N. Hong, J.-K. Park, and J. Ko, "Influence of aggregate coated with modified sulfur on the properties of cement concrete," *Materials*, vol. 7, no. 6, pp. 4739–4754, 2014.

[14] W.-W. Li, W.-M. Ji, Y.-C. Wang, Y. Liu, R.-X. Shen, and F. Xing, "Investigation on the mechanical properties of a cement-based material containing carbon nanotube under drying and freeze-thaw conditions," *Materials*, vol. 8, no. 12, pp. 8780–8792, 2015.

[15] Y. Tan and M. Guo, "Micro- and Nano-Characteration of Interaction Between Asphalt and Filler," *Journal of Testing and Evaluation*, vol. 42, no. 5, pp. 1089–1097, 2014.

[16] S. Guo, Q. Dai, X. Sun, and Y. Sun, "Ultrasonic scattering measurement of air void size distribution in hardened concrete samples," *Construction and Building Materials*, vol. 113, pp. 415–422, 2016.

[17] M. A. B. Promentilla and T. Sugiyama, "X-ray microtomography of mortars exposed to freezing-thawing action," *Journal of Advanced Concrete Technology*, vol. 8, no. 2, pp. 97–111, 2010.

[18] H. Xu, W. Guo, and Y. Tan, "Internal structure evolution of asphalt mixtures during freeze-thaw cycles," *Materials and Design*, vol. 86, pp. 436–446, 2015.